

EPiC Series in Computing

Volume 114, 2026, Pages 224–240

Proceedings of the Workshop on Mathematical Modeling and Scientific Computing



Computational Approach for Exploring the Characteristics of Quorum-Mediated Signaling Dynamics during Bacterial Biofilm Growth

Samvel K. Sarukhanian[1], Christina Kuttler[2], and Anna G. Maslovskaya[1]

[1] Laboratory for Simulation and Intelligent Analysis of Complex Systems, Innopolis University, Innopolis, Russia
sa.sarukhanian@innopolis.ru, a.maslovskaya@innopolis.ru

[2] Department of Mathematics, Technical University of Munich, Garching, Germany
kuttler@ma.tum.de

Abstract

This paper presents an extension of a hybrid cellular automaton model for spatial bacterial biofilm growth with quorum sensing regulation. The model is formulated on a two-dimensional hexagonal lattice and combines discrete biomass dynamics with nutrient and acyl-homoserine lactone (AHL) fields, Monod-type growth kinetics, diffusion-based transport, and a nonlinear Hill-type quorum sensing response. The main extension is a transient additional AHL degradation mechanism that modifies the signaling field without directly suppressing biomass growth, thereby affecting biofilm development through quorum sensing dependent biomass redistribution. The simulation algorithm was modified accordingly by introducing a time-dependent degradation stage while preserving the baseline transport, growth, signal-production, and redistribution procedures. The model and the modified algorithm were implemented in C# within the Unity environment, where the developed application supports repeated stochastic simulations and systematic variation of intervention parameters. Numerical experiments show that the effect of transient AHL degradation depends strongly on its temporal placement relative to the development of the signaling field. The most pronounced changes in cumulative AHL exposure and bottom-surface coverage occur for intermediate onset times of approximately 12.5–15 h. Increasing the intervention duration from 10 to 15 h broadens this effective interval, whereas further increases in the additional degradation rate above a moderate level produce progressively smaller changes. The correspondence between the AHL response and surface-coverage maps indicates that temporary modification of signaling dynamics can lead to persistent changes in bacterial surface colonization within the simulated biofilm system.

1 Introduction

Bacterial biofilms are spatially organized communities of microorganisms attached to biotic or abiotic surfaces and, as a rule, embedded in an extracellular polymeric matrix. The transition from a planktonic state to a biofilm lifestyle is accompanied by substantial changes in cell

V. Turova, A. Kovtanyuk, A. Maslovskaya and J. Zimmer (eds.), MMSC 2026 (EPiC Series in Computing, vol. 114), pp. 224–240

physiology, the character of intercellular interactions, and the distribution of metabolic activity within the community [4, 10]. The biofilm matrix not only provides mechanical stability and adhesion but also creates a local microenvironment in which extracellular enzymes, nutrients, and signaling molecules are retained [7]. As a result, the advantageous biofilm lifestyle is one of the dominant forms of microbial organization in natural ecosystems [8].

An important feature of biofilms is their pronounced spatial heterogeneity. Diffusion of oxygen and nutrients, their local consumption, and the accumulation of metabolites and signaling compounds generate complex spatial gradients inside the biofilm, so neighboring cells may exist in substantially different physiological states [24]. Biofilm spatial organization is formed under the influence of numerous interacting factors and therefore cannot be characterized solely by total biomass or population-averaged quantities. Experimental studies of bacterial communities demonstrate complex architectural transitions during biofilm growth [5], whereas mathematical models reveal a close relationship between structure geometry, mass transfer, hydrodynamic conditions, and local growth and substrate-consumption processes [6]. Such coupling is particularly important when modelling external influences capable of modifying mechanisms of collective bacterial behavior.

A wide range of mathematical approaches is used to investigate the spatiotemporal evolution of biofilms. Continuous models based on systems of ordinary and partial differential equations make it possible to describe growth, substrate consumption, and mass transfer using reaction–diffusion-type equations [6]. However, such models do not always explicitly account for the stochastic nature of complex structure formation, local division events, and random choices of spatial spreading direction. Individual-based and cellular automaton models provide an alternative approach, in which spatial evolution emerges from local interaction rules applied to individual cells or discrete biomass elements [1, 11, 19, 20]. Hybrid models occupy a special position because they combine discrete biomass dynamics with a continuous or discretized description of diffusion processes. The classical study by Picioreanu et al. demonstrated that biofilm shape, roughness, and porosity can be reproduced using a hybrid differential-discrete model [19], while subsequent individual-based and three-dimensional models extended this approach to more complex multicomponent systems [1, 11]. Cellular automaton methods also provide an efficient framework for modelling bacterial division, spreading, and structural rearrangement [20, 23].

Quorum-sensing mechanisms have also been incorporated into mathematical models of bacterial populations and biofilms. In one of the early fundamental mathematical models, Dockery and Keener showed that signal accumulation and changes in bacterial population density can determine the global state of the system and induce a transition between quorum sensing inactive and quorum sensing active regimes [2]. Reaction–diffusion models were subsequently developed to account for signal production, transport, degradation, and the effects of spatial population organization [18, 25]. The review by Pérez-Velázquez et al. systematized the principal classes of mathematical quorum sensing models in which population growth, signal transport, and regulatory feedback are considered jointly [18]. Hybrid and fractional-order approaches have also been applied to investigate signal transport, stochastic population dynamics, and the influence of external factors [12, 13].

At the biological level, quorum sensing is an important mechanism of intercellular communication that can influence biofilm development. Bacterial cells produce, release, and detect signaling molecules known as autoinducers; changes in their local concentrations are used to coordinate gene expression and collective population behavior [15, 17, 26]. In many Gram-negative bacteria, including *Pseudomonas aeruginosa*, N-acyl homoserine lactones (AHLs) interacting with LuxR-type proteins are especially important. In *P. aeruginosa*, the Las and Rhl systems

form part of a complex hierarchical signaling network regulating a wide range of processes related to collective behavior, virulence, and biofilm formation [14]. Thus, the concentration of signaling molecules represents an independent dynamic variable linking the local state of bacterial cells to the collective response of the population.

The presence of a communication mechanism controlling collective population behavior makes quorum sensing an attractive target for external intervention. One major direction is the disruption of bacterial communication, commonly referred to as quorum quenching (QQ). QQ mechanisms include inhibition of signal synthesis, competitive or noncompetitive inhibition of receptors, chemical transformation of autoinducers, and enzymatic signal degradation [9]. The feasibility of suppressing AHL dependent quorum sensing through enzymatic signal degradation was experimentally demonstrated by Dong et al. using an AHL lactonase [3]. Recent reviews of quorum quenching discuss lactonases, acylases, oxidoreductases, and other enzymes capable of reducing the effective signal concentration and modifying the biofilm phenotype without directly exerting a bactericidal effect [9, 16, 21]. This fundamentally distinguishes QQ from conventional interventions aimed directly at bacterial viability.

At the same time, the effectiveness of quorum sensing disruption is determined not only by the magnitude of signal suppression but also by the timing and duration of the intervention. A biofilm is a nonstationary system: cell density, AHL production intensity, diffusion processes, nutrient availability, and the local quorum sensing state continuously change over time. Current concepts of quorum sensing emphasize that the signaling response depends not only on cell number but also on spatial population organization, mass transfer, fluid flow, and local biofilm structure [15, 17]. Consequently, interventions of equal intensity applied before substantial AHL accumulation, directly within the quorum sensing transition region, or after formation of the collective response may lead to markedly different outcomes.

Most quorum-quenching studies focus on identifying molecular targets, searching for inhibitors and enzymes, comparing signal-disruption mechanisms, and evaluating final antibiofilm or antivirulence effects [3, 9, 16, 21]. Considerably less attention in mathematical modelling has been given to the temporal organization of finite-duration interventions relative to the intrinsic dynamics of the quorum-sensing transition. In the present study, the intervention is represented as an idealized time-limited increase in the AHL degradation rate that is maintained over a prescribed interval and then returned to its baseline value. This formulation is intended to describe a controlled period of enhanced signal degradation rather than the instantaneous appearance and disappearance of a specific inhibitor. Within such a framework, intervention intensity, onset time, and duration are independent control parameters. An early intervention may end before substantial AHL accumulation occurs, an intervention applied near the QS-transition region may strongly alter the signaling dynamics, whereas a late intervention may begin after a considerable part of QS-dependent spatial restructuring has already taken place.

In our previous studies, we developed a cellular automaton methodology for modelling the spatial evolution of biofilms while accounting for nutrient limitation, diffusion processes, local division, and biomass redistribution [22, 23]. In the present work, this model is extended by a mechanism of transient signal suppression and used to investigate quorum sensing regulated biofilm evolution on a two-dimensional hexagonal lattice. The hybrid model combines discrete biomass dynamics with continuous nutrient and AHL fields; signal production depends on the biomass state, AHL diffuses through the computational domain and undergoes degradation, and the local quorum sensing response is represented by a nonlinear Hill function. The signaling concentration is directly coupled to the mechanism of spatial biomass spreading, so modification of the AHL field can influence biofilm morphology without directly reducing the basic metabolic growth rate.

The aim of this study is to investigate the effect of transient AHL suppression on the spatiotemporal evolution of a bacterial biofilm and to determine the relationship between intervention start time, duration, and intensity. We consider the hypothesis that a critical temporal window exists in association with the natural transition of the system into a quorum sensing active state. To test this hypothesis, a series of computational experiments is performed in which the intervention start time, duration, and intensity are varied. The analysis focuses on mean AHL dynamics, cumulative AHL exposure, bottom-surface coverage and representative spatial configurations. This approach makes it possible to distinguish between the immediate effect of intervention on the signaling field and its long-term influence on the formation of the spatial biofilm structure.

2 Model description

2.1 Conceptual formulation of the model

The model uses three local state variables: biomass B, nutrient concentration N, and AHL concentration U. Nutrient availability controls biomass growth, biomass produces AHL, and the local AHL level regulates quorum sensing dependent biomass redistribution. Figure 1 summarizes this feedback and the intervention considered in this work.

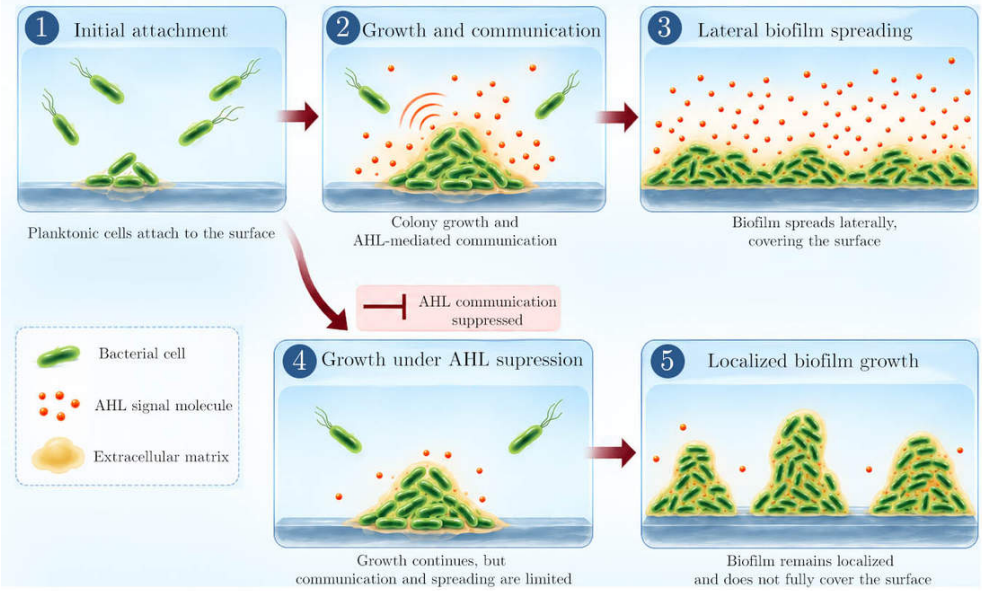


Figure 1: Conceptual scheme of biofilm development without and with transient additional AHL degradation.

Initially, a small number of colonies is placed near the bottom surface. Biomass grows by consuming nutrient and produces AHL. As the local AHL concentration increases, the quorum sensing dependent redistribution rule becomes more active and biomass spreads to new lattice sites. Without additional degradation, separated colonies can merge and form a more continuous layer along the bottom surface. During the intervention, the AHL degradation rate is increased for a prescribed time interval. Biomass growth is not directly reduced. The intervention acts

only through the signaling field; any change in biofilm morphology is therefore caused by the altered quorum sensing dependent redistribution dynamics. After the intervention ends, the model returns to the baseline AHL degradation rate. From a biological perspective, the imposed increase in AHL degradation can be interpreted as an idealized representation of an external intervention that temporarily reduces the lifetime of signaling molecules in the biofilm environment. Such an effect may arise, for example, from a controlled change in environmental conditions, including pH, which can accelerate AHL hydrolysis, or from externally maintained quorum-quenching activity that enhances signal removal. The present model does not explicitly describe the dynamics of pH, enzyme concentration, or a particular chemical agent. Instead, these effects are represented through an effective increase in the AHL degradation rate over a prescribed time interval. Thus, the investigated parameters characterize the timing and strength of signal attenuation rather than the dose or pharmacokinetics of a specific treatment.

2.2 Computational geometry and indexing

The computational domain is a two-dimensional regular hexagonal lattice. The lattice is stored in a rectangular array with staggered rows. Each lattice unit $C_{i,j}$ stores nutrient concentration $N_{i,j}$, AHL concentration $U_{i,j}$, and biomass $B_{i,j}$ (Fig. 2). Here and below, indices run over $i = 0, \ldots, W-1$ and $j = 0, \ldots, H-1$, and sums over i, j are taken over all corresponding lattice sites unless otherwise stated. A lattice unit is a spatial compartment and does not represent a single bacterial cell. The parameter c_0 in Table 1 characterizes the baseline nutrient initialization.

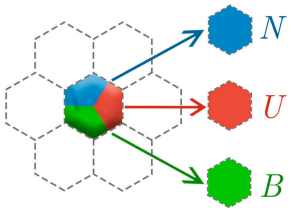
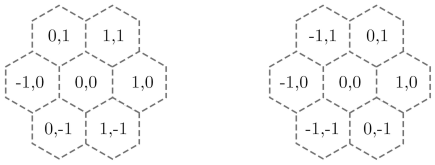


Figure 2: Local state of a hexagonal lattice unit. N: nutrient concentration; U: AHL concentration; B: biomass.

The two patterns alternate between successive rows (Fig. 3). The domain boundaries are treated as fixed.



(a) (b)

Figure 3: The two six-neighbor configurations corresponding to the staggered row types used for orthogonal indexing of the hexagonal lattice.

The six-neighbor stencil therefore depends on row parity. For the two row types, the neighbor

sets are

$$\mathcal{N}_{i,j}^{\mathrm{A}} = \{(i-1,j),(i+1,j),(i,j+1),(i+1,j+1),\\ (i,j-1),(i+1,j-1)\},$$
$$\mathcal{N}_{i,j}^{\mathrm{B}} = \{(i-1,j),(i+1,j),(i-1,j+1),(i,j+1),\\ (i-1,j-1),(i,j-1)\}.$$

2.3 Growth, signaling, and redistribution

Nutrient-dependent growth is described by Monod kinetics,

$$f_N(N_{i,j}) = \mu_{\max}\frac{N_{i,j}}{K_N + N_{i,j}}, \tag{1}$$

where $\mu_{\max}$ is the maximum specific growth rate and K_N is the half-saturation constant. The biomass increment requested over one time step is

$$\Delta B_{i,j}^{\mathrm{req}} = f_N(N_{i,j}^{\mathrm{diff}})B_{i,j}^{n}\Delta t, \tag{2}$$

Nutrient consumption is related to biomass growth by the biomass–nutrient yield coefficient Y_{BN}. Since the local consumption cannot exceed the nutrient available after diffusion, the consumed quantity is limited according to

$$\Delta N_{i,j}^{\mathrm{cons}} = \min\left\{N_{i,j}^{\mathrm{diff}}, \frac{\Delta B_{i,j}^{\mathrm{req}}}{Y_{BN}}\right\}, \tag{3}$$

with the nutrient and realized biomass updates

$$N_{i,j}^{\mathrm{grow}} = N_{i,j}^{\mathrm{diff}} - \Delta N_{i,j}^{\mathrm{cons}}, \tag{4}$$
$$B_{i,j}^{\mathrm{grow}} = B_{i,j}^{n} + Y_{BN}\Delta N_{i,j}^{\mathrm{cons}}. \tag{5}$$

Thus, biomass growth is constrained by local nutrient availability rather than allowing the nutrient concentration to become negative.

The local quorum sensing response is described by the Hill function

$$H(U_{i,j}) = \frac{U_{i,j}^{q}}{U_{\mathrm{th}}^{q} + U_{i,j}^{q}}, \tag{6}$$

where U_{th} is the quorum sensing threshold and q is the Hill exponent. In the present simulations, the AHL-response Hill exponent is $q = 1.3$; it does not modify the standard Monod law in Eq. (1). AHL production depends on local biomass, nutrient availability, and the current quorum sensing state,

$$P_U(B,N,U) = B\left[\alpha + \beta H(U)\right]\frac{N}{K_N + N} \tag{7}$$

Using a direct AHL-production formulation motivated by the baseline CiBaM framework, Eq. (7) defines a local production *rate*, not an increment associated with nutrient consumption. The nutrient-dependence is represented by the Monod saturation factor $N/(K_N + N)$, while the

dependence on biomass is linear. For a simulation step of length Δt (in seconds), the AHL increment due to local production at an occupied lattice site is

$$\Delta U_{i,j}^{\mathrm{prod}} = \Delta t\, P_U\left(B_{i,j}^{\mathrm{grow}}, N_{i,j}^{\mathrm{grow}}, U_{i,j}^{\mathrm{deg}}\right), \tag{8}$$

where the arguments are taken at the local production stage. The corresponding field update is

$$U_{i,j}^{n+1} = U_{i,j}^{\mathrm{deg}} + \Delta U_{i,j}^{\mathrm{prod}}. \tag{9}$$

Here U^{deg} is the AHL field after diffusion and signal degradation. At unoccupied lattice sites, $B = 0$ and no AHL is produced locally. The factor Δt appears exactly once in the production update; in particular, the production term is not multiplied by the nutrient-consumption increment ΔN^{cons}. This avoids introducing an unintended quadratic dependence on biomass. The quorum-regulated probability of basal spreading uses a separate Hill response from the AHL-production response in Eq. (6). Let $\widetilde{U}_{i,j} = U_{i,j}/s_U$ be the locally normalized AHL value. The spreading response and its associated probability are

$$H_{\mathrm{sp}}(U_{i,j}) = \frac{\widetilde{U}_{i,j}^{q_{\mathrm{sp}}}}{\widetilde{U}_{i,j}^{q_{\mathrm{sp}}} + U_{\mathrm{th}}^{q_{\mathrm{sp}}}}, \tag{10}$$

$$p(U_{i,j}) = p_{\min} + (p_{\max} - p_{\min}) H_{\mathrm{sp}}(U_{i,j}), \tag{11}$$

where $p_{\min} = 0$, $p_{\max} = 0.05$, $q_{\mathrm{sp}} = 4$, and $s_U = 1$. The spreading exponent $q_{\mathrm{sp}} = 4$ is distinct from the AHL-production exponent $q = 1.3$. In accordance with Fig. 4, a basal spreading attempt is triggered only if the local concentration exceeds U_{th} and an independent uniform random draw $r \in [0, 1)$ satisfies $r < p(U_{i,j})$. Standard neighboring-site division is not subject to this surface-spreading test.

2.4 Diffusion transport and boundary conditions

The nutrient and AHL fields undergo separate diffusion updates. The effective diffusion parameters D_N and D_U in this work are the numerical coefficients used by the simulation, expressed in lattice-units squared per second (with $h = 1$ lattice unit), not diffusivities quoted in physical $\mathrm{m}^2\,\mathrm{s}^{-1}$. At the continuum level in grid coordinates, the diffusion subproblems are

$$\frac{\partial N}{\partial t} = D_N \nabla^2 N, \tag{12}$$

$$\frac{\partial U}{\partial t} = D_U \nabla^2 U. \tag{13}$$

Nutrient consumption, AHL production, and degradation are applied as distinct reaction updates and are not included in Eqs. (12)–(13).

In all reported simulations, diffusion was computed using the three-direction implicit splitting scheme (HexADI) on the staggered hexagonal grid. The directional graph-difference operators are defined by

$$(\mathcal{L}_a F)_{i,j} = \sum_{(k,l)\in\mathcal{N}_{i,j}^{(a)}} (F_{k,l} - F_{i,j}), \qquad \mathcal{L}_{\mathrm{hex}} = \sum_{a=1}^{3} \mathcal{L}_a. \tag{14}$$

Here, F denotes either N or U, while $\mathcal{N}_{i,j}^{(a)}$ represents the set of at most two neighboring sites along lattice axis $a \in \{1, 2, 3\}$.

In this three-direction hexagonal scheme, each successive implicit sweep has the form

$$(I - r_F \mathcal{L}_a) F^{(a)} = F^{(a-1)}, \qquad r_F = \frac{2 D_F^{\text{solver}} \Delta t}{3h^2}, \quad a = 1, 2, 3, \tag{15}$$

where $F^{(0)}$ is the field before diffusion, h is the numerical lattice spacing, and D_F^{solver} is the diffusion coefficient passed to the solver. The three sweep directions are horizontal and the two diagonal axes. Their order is reversed on alternating time steps. Each one-dimensional implicit system is tridiagonal and is solved using the Thomas algorithm.

For both concentration fields, the diffusion update imposes homogeneous no-flux boundary conditions on the computational domain,

$$\left.\frac{\partial N}{\partial \mathbf{n}}\right|_{\partial\Omega} = 0, \qquad \left.\frac{\partial U}{\partial \mathbf{n}}\right|_{\partial\Omega} = 0, \tag{16}$$

where $\mathbf{n}$ is the outward normal. In the hexagonal operator these are implemented by omitting neighbors outside the domain, so the diagonal coefficient in a directional solve is $1 + r_F d_{i,j}^{(a)}$, where $d_{i,j}^{(a)} = |\mathcal{N}_{i,j}^{(a)}|$.

2.5 Transient AHL degradation

Baseline AHL degradation is implemented as an exponential loss over one simulation step. According to the update sequence in Fig. 4, let $U_{i,j}^{\text{diff}}$ denote the field after diffusion but before degradation and the subsequent local production update. In the untreated case, the degradation substep is

$$U_{i,j}^{\text{deg}} = U_{i,j}^{\text{diff}} \exp(-k_{\text{deg}} \Delta t_h)\,. \tag{17}$$

where k_{deg} is the baseline degradation rate expressed in h^{-1}. The simulation time step Δt is given in seconds; therefore, $\Delta t_h = \Delta t/3600$ is the corresponding time interval in hours.

For the intervention, define

$$I^n = \begin{cases} 1, & D_{\text{start}} \le t_n < D_{\text{start}} + D_{\text{duration}}, \\ 0, & \text{otherwise.} \end{cases} \tag{18}$$

The effective degradation rate is then

$$k_{\text{eff}}^n = k_{\text{deg}} + D_{\text{amount}} I^n, \tag{19}$$

and the AHL loss step becomes

$$U_{i,j}^{\text{deg}} = U_{i,j}^{\text{diff}} \exp(-k_{\text{eff}}^n \Delta t_h)\,. \tag{20}$$

Here $t_n = n\Delta t_h$ and the intervention parameters D_{start} and D_{duration} are expressed in hours. Thus, D_{amount} is an additional degradation rate used only during the intervention window; it is not interpreted as a drug concentration. The resulting field U^{deg} then enters the local production update in Eqs. (8)–(9).

For clarity, combining the diffusion, degradation, and direct CiBaM production stages gives the complete AHL update

$$\begin{aligned} U_{i,j}^{n+1} = {} & U_{i,j}^{\text{diff}} \exp(-k_{\text{eff}}^n \Delta t_h) \\ & + \Delta t\, B_{i,j}^{\text{grow}} \left[\alpha + \beta H\left(U_{i,j}^{\text{deg}}\right)\right] \frac{N_{i,j}^{\text{grow}}}{K_N + N_{i,j}^{\text{grow}}}. \end{aligned} \tag{21}$$

Thus, the intervention changes AHL loss, whereas production remains governed by Eq. (7). In particular, $D_{\text{amount}} = 0$ recovers the untreated case.

3 Algorithm and software implementation

The numerical experiments were performed with a C# implementation of the hybrid cellular automaton in Unity. Biomass is updated on the regular hexagonal lattice, whereas separate procedures advance the nutrient and AHL fields. Visualization and data logging are kept separate from the physical state updates, which allows the same simulation core to be used for repeated parameter sweeps.

The simulation procedure is summarized in Fig. 4, with transport and numerical diffusion relations given in Eqs. (12)–(16).

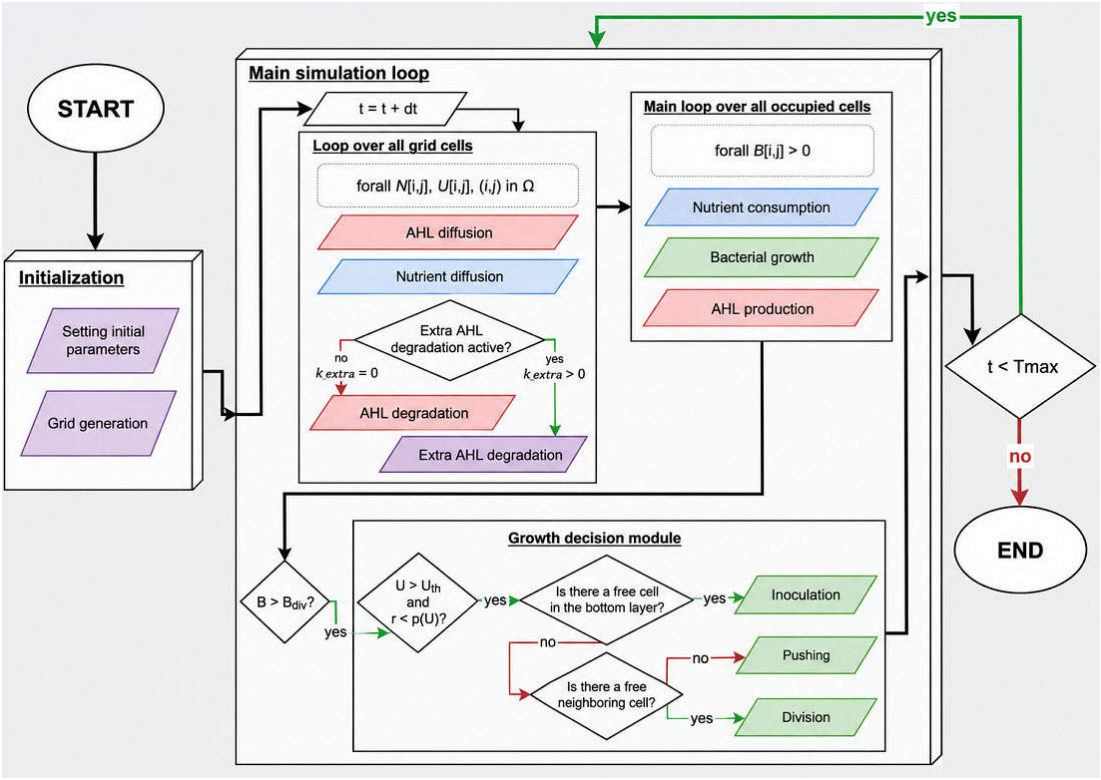


Figure 4: Computational flowchart of the hybrid cellular automaton with transient AHL degradation. The variables N, U, and B denote nutrient concentration, AHL concentration, and biomass. Diffusion and signal degradation are applied over the entire lattice; consumption, growth, and AHL production are evaluated at occupied sites. The intervention contributes $D_{\text{amount}} I^n$ to the baseline degradation rate, and this additional term is zero outside the intervention window. The subsequent redistribution stage is controlled by the local signaling response and the availability of free sites.

In Figure 4, the computational domain is $\Omega = \{0, \ldots, W-1\} \times \{0, \ldots, H-1\}$, and its occupied subset at time t_n is $\Omega_B^n = \{(i,j) \in \Omega : B_{i,j}^n > 0\}$. The division threshold B_{div} specifies the minimum local biomass for initiating a division attempt. The quantity $r \sim \mathcal{U}(0,1)$ is a uniform random draw, whereas $p(U) \in [0,1]$ denotes the local, quorum-sensing-dependent probability used in the surface-spreading test in Eq. (11). The test additionally requires $U > U_{\text{th}}$, as depicted in the flowchart. The symbols U_{th} and $t_{\max}$ are the QS threshold and the simulation

horizon, respectively. The extra degradation contribution is $k^n_{\text{extra}} = D_{\text{amount}} I^n$; thus $k^n_{\text{extra}} = 0$ when the intervention is inactive.

After initialization, one iteration proceeds as follows. First, the nutrient and AHL fields are advanced by diffusion across Ω, using Eqs. (12)– (15) and the no-flux conditions in Eq. (16). Second, baseline AHL degradation is applied, together with the additional rate when active, according to Eqs. (18)–(20). Third, nutrient consumption and biomass growth are evaluated at occupied sites, as described by Eqs. (1)– (5). The production term P_U then contributes directly to the AHL field through Eqs. (7)–(9); the combined update is given in Eq. (21). Finally, the QS-dependent surface-spreading condition uses the local AHL response and random draw r; when no suitable basal site is selected, the algorithm attempts division into a free neighbor or the pushing procedure, subject to the local biomass and occupancy conditions. Newly created biomass states are committed at the end of the iteration.

4 Simulation of biofilm growth under transient quorum sensing suppression

The additional AHL degradation was investigated by varying three intervention parameters: the onset time D_{start}, duration D_{duration}, and intensity D_{amount}. Their respective sets of values were

$$D_{\text{start}} \in \{5, 7.5, 10, 12.5, 15, 17.5\}\,\text{h}, \tag{22}$$

$$D_{\text{duration}} \in \{10, 15\}\,\text{h}, \tag{23}$$

$$D_{\text{amount}} \in \{0.5, 1.0, 1.5, 2.0, 2.5, 3.0, 3.5\}\,\text{h}^{-1}. \tag{24}$$

This gives $6 \times 2 \times 7 = 84$ treated parameter combinations. Each combination was simulated ten times. The same set of ten random seeds was reused across parameter combinations, and ten untreated runs were added as a reference. The full data set therefore contains 850 simulations.

The experiments used a 200×130 lattice, a time step of 25 s, and a simulation horizon of 42 h. The fixed parameters are listed in Table 1. Most kinetic, transport, and quorum-sensing parameters were retained from the previously developed baseline model [22, 23], whereas the remaining parameters define the computational setup of the present study. Biomass, nutrient, and AHL concentrations in the cellular automaton are represented in normalized model units; c_0, K_N, and U_{th} therefore refer to normalized concentration values. Under this convention, Y_{BN} is a dimensionless biomass–nutrient yield and α, β have units of s^{-1} for the adopted production law. Here lu denotes one lattice-length unit. The diffusion coefficients in Table 1 are the values set in the numerical model: $D_N = 0.84$ and $D_U = 0.1112$ in lattice-units squared per second. In the CiBaM implementation used for the diffusion-solver description, the coefficient passed to the HexADI directional sweeps is $D_F^{\text{solver}} = D_F/4$. Thus $D_N^{\text{solver}} = 0.21$ and $D_U^{\text{solver}} = 0.0278$, with numerical grid spacing $h = 1$ lattice unit. No direct equivalence with an SI physical diffusion coefficient is assumed without specifying the physical length corresponding to one lattice unit.

The intervention parameters D_{start}, D_{duration}, and D_{amount} are varied over the sets given above and therefore are not listed among the fixed parameters in Table 1. The random draw r, the indicator I^n, and the intermediate states in the split-step updates are not independent fixed parameters.

Figure 5 provides a qualitative comparison of untreated and treated spatial development over the same observation times.

The principal outputs analyzed in the following results are the domain-mean AHL

Table 1: Fixed parameters of the computational experiment and their rationale.

Parameter	Value	Meaning	Origin / rationale
$W \times H$	200×130	lattice dimensions	computational domain
Δt	25 s	time step	fixed numerical time step
h	1 lu	spacing of the lattice	
c_0	0.2	initial nutrient (normalized model units)	experiment setting
$\mu_{\max}$	$1.67 \times 10^{-4}\,\mathrm{s}^{-1}$	maximum specific growth rate	[23]
K_N	0.21	Monod half-saturation (normalized nutrient units)	[22]
Y_{BN}	0.5	biomass–nutrient yield (dimensionless in normalized units)	[22]
B_{div}	1	division threshold (normalized biomass)	[23]
D_N	$0.84\,\mathrm{lu}^2\,\mathrm{s}^{-1}$	nutrient diffusion, simulation setting	[23]
D_U	$0.1112\,\mathrm{lu}^2\,\mathrm{s}^{-1}$	AHL diffusion, simulation setting	[22]
α	$1.0 \times 10^{-4}\,\mathrm{s}^{-1}$	basal AHL production, normalized units	[22]
β	$1.39 \times 10^{-3}\,\mathrm{s}^{-1}$	QS-induced AHL production, normalized units	[22]
k_{deg}	$0.95\,\mathrm{h}^{-1}$	baseline AHL degradation rate	baseline signaling condition
s_U	1	AHL normalization factor (dimensionless)	[22]
q_{sp}	4	Hill exponent for spreading (dimensionless)	[22]
$p_{\min}$	0	minimum spreading probability (dimensionless)	[22]
q	1.3	Hill exponent (dimensionless)	[22]
$p_{\max}$	0.05	maximum surface-spreading probability (dimensionless)	[22]
U_{th}	6.5×10^{-5}	QS threshold (normalized AHL)	[22]
n_0	5	number of initial colonies (dimensionless count)	fixed initial condition
$t_{\max}$	42 h	simulation horizon	covers main growth stage

concentration and bottom-surface coverage. The mean AHL concentration is

$$\overline{U}(t) = \frac{1}{WH} \sum_{i=0}^{W-1} \sum_{j=0}^{H-1} U_{i,j}(t). \tag{25}$$

Bottom-surface coverage is defined as

$$C(t) = \frac{1}{W} \sum_{i=0}^{W-1} \mathbf{1}_{\{B_{i,0}(t)>0\}}, \tag{26}$$

where the indicator equals 1 for an occupied bottom-surface site and 0 otherwise.

The coverage metric $C(t)$ characterizes bacterial colonization of the basal surface of the computational domain. It should not be interpreted as a direct measure of total biofilm biomass, biofilm thickness, or the overall spatial extent of the bacterial community. Here, $C(t)$ is used

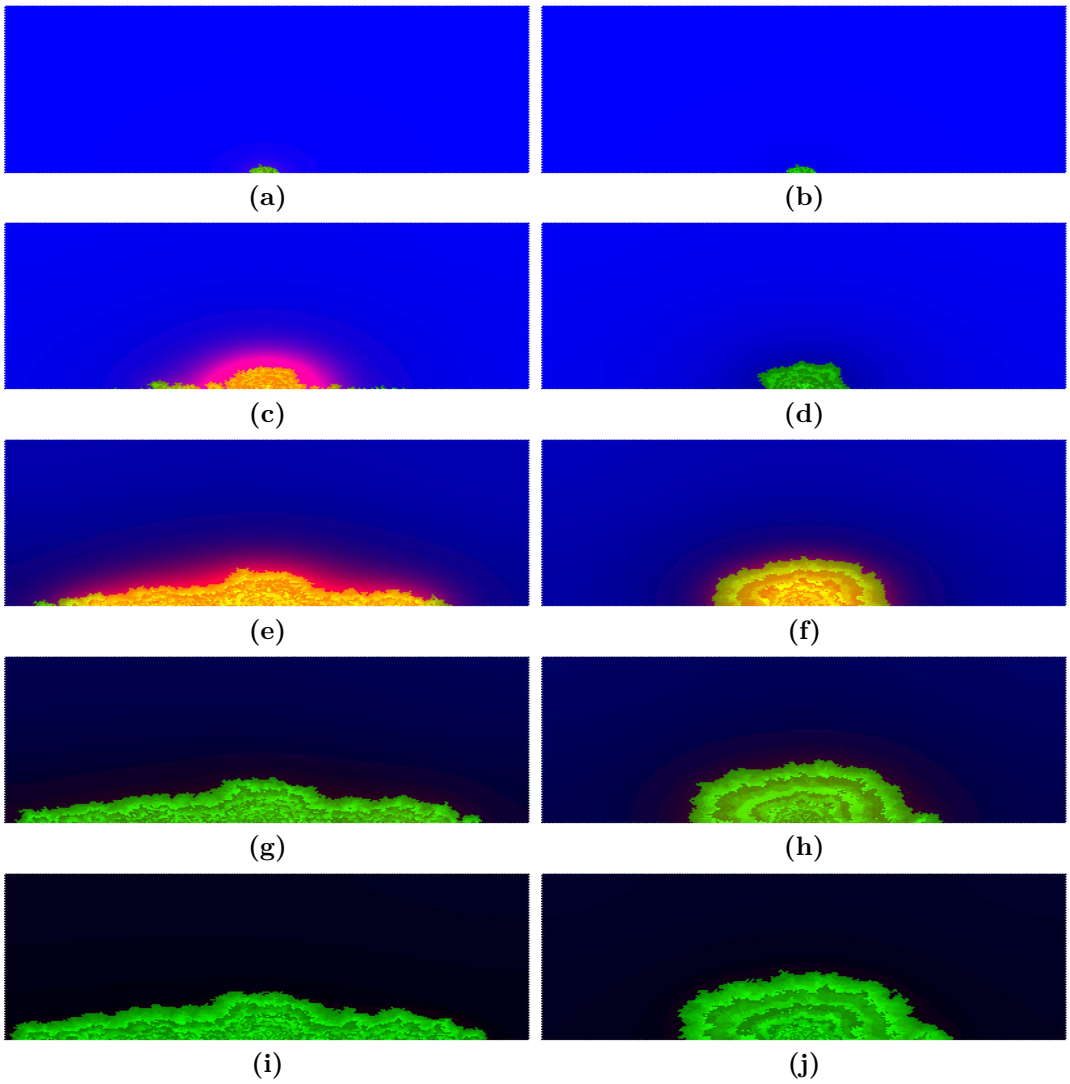


Figure 5: Spatial evolution of the simulated biofilm without additional AHL degradation (left column) and under a representative transient-degradation regime with $D_{start} = 7.5\,\mathrm{h}$, $D_{duration} = 15\,\mathrm{h}$, and $D_{amount} = 1\,\mathrm{h}^{-1}$ from the present factorial study (right column). Snapshots correspond to $t = 8, 16, 24, 32$, and $40\,\mathrm{h}$.

specifically to quantify changes in basal surface colonization caused by transient AHL degradation. The spatial configurations in Fig. 5 provide complementary qualitative information about the biomass distribution within the computational domain.

Cumulative AHL exposure was calculated from the recorded mean-AHL time series using the trapezoidal rule,

$$A_U = \int_0^{t_{max}} \overline{U}(t)\, dt, \tag{27}$$

over the recorded simulation interval. All reported means and standard deviations are calculated

over the repeated runs.

Figure 6 shows that the same 10-h intervention produces different AHL trajectories depending on its start time. At 10 h, the signal can recover after the intervention ends. Starting at 15 h overlaps a later part of the high-AHL interval and produces a deeper reduction for the moderate and high rates shown. By 17.5 h, much of the initial AHL rise has already occurred before the intervention starts.

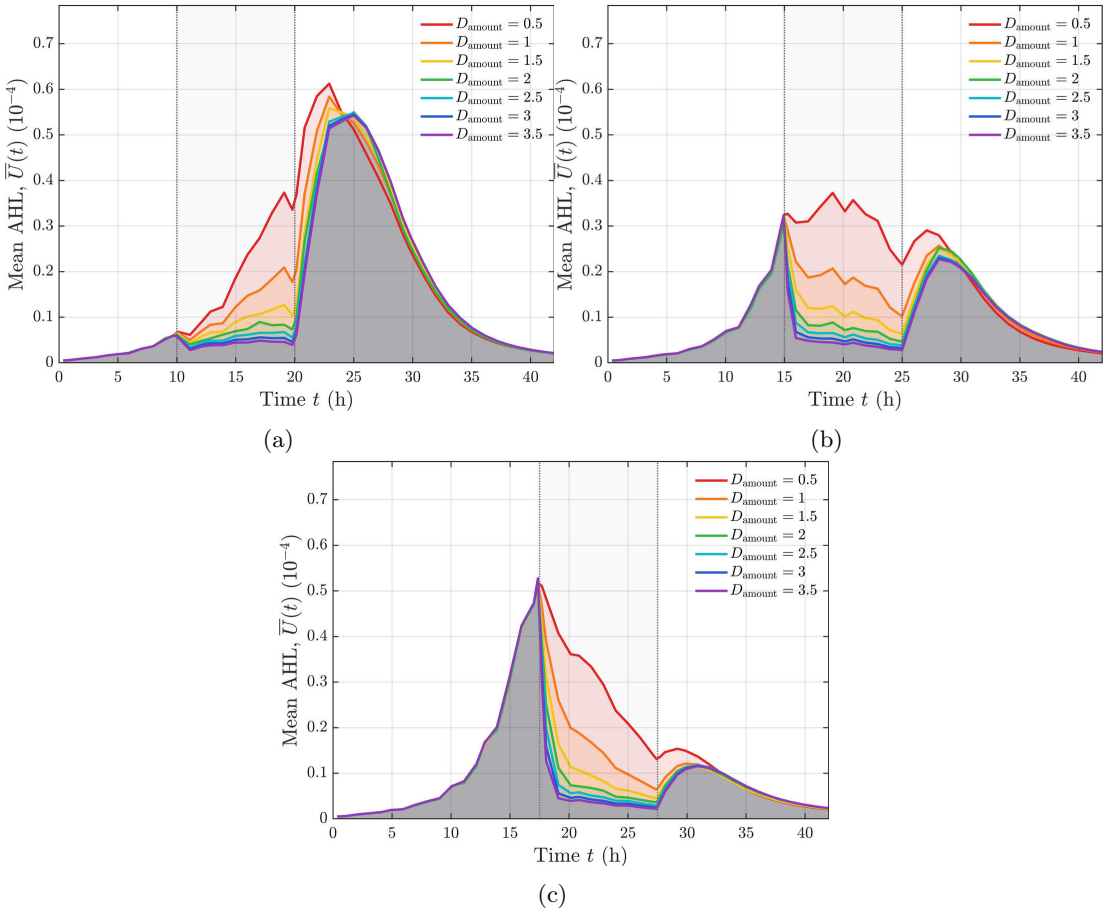


Figure 6: Domain-mean AHL concentration $\overline{U}(t)$ for several additional-degradation rates at a fixed intervention duration of 10 h and three onset times: (a) 10 h, (b) 15 h, and (c) 17.5 h.

The untreated simulations provide a reference for the characteristic timing of AHL accumulation. The first recorded crossing of U_{th} by the domain-mean AHL concentration occurred at 8.51 ± 0.74 h. Because the regulatory function is evaluated locally, this domain-average crossing is used only as a global timing indicator and not as a strict quorum sensing switching time for every occupied site. Complete bottom-surface coverage was reached at 16.94 ± 0.91 h, and all ten untreated realizations had 100% final coverage at 42 h.

Figure 7 summarizes the AHL response over the complete onset-time–intensity grid for the two intervention durations. A pronounced low-AHL region is concentrated at intermediate onset times, approximately between 12.5 and 15 h, rather than at the earliest or latest interventions.

Increasing the duration from 10 to 15 h broadens this region along the onset-time axis, indicating that a longer intervention is less sensitive to small shifts in its starting time. The maps also show diminishing returns with increasing suppression intensity: most of the additional reduction is achieved by approximately $D_{\text{amount}} = 1.5$, whereas larger values change the response more gradually. This pattern indicates that timing and duration cannot be compensated for simply by increasing intervention intensity.

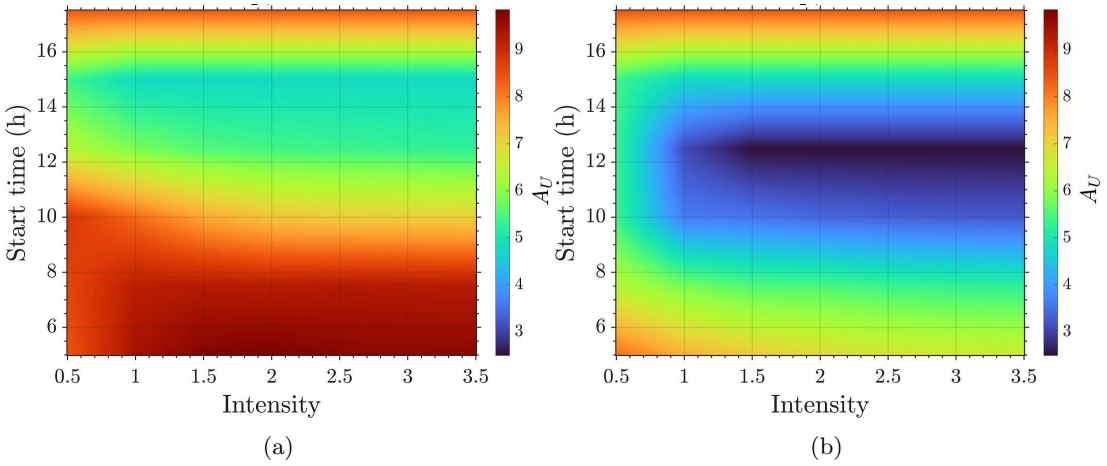


Figure 7: Cumulative AHL exposure A_U as a function of intervention start time and additional degradation rate for intervention durations of (a) 10 h and (b) 15 h.

The final-coverage maps in Fig. 8 show how changes in AHL signaling dynamics affect the degree of bacterial colonization along the bottom boundary of the computational domain.

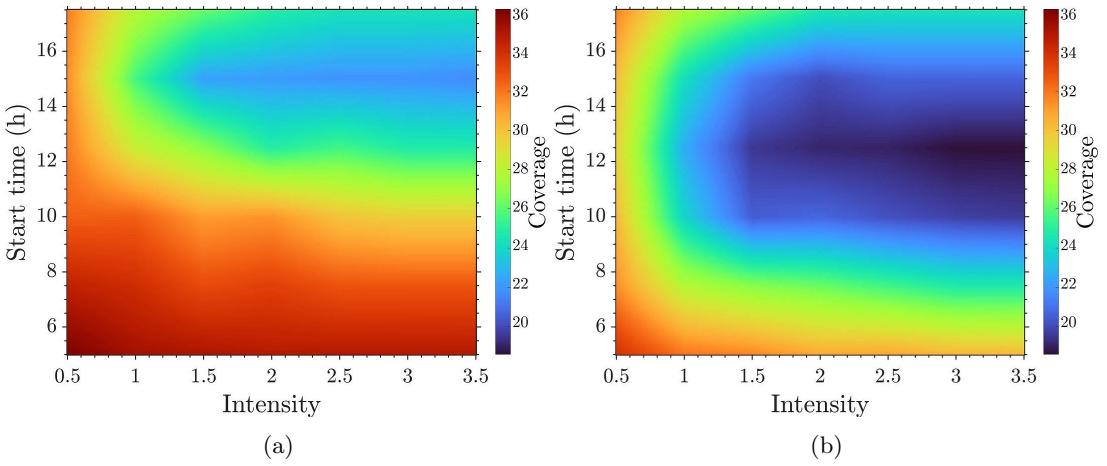


Figure 8: Final bottom-surface coverage $C(t_{\max})$ as a function of intervention start time and additional degradation rate for durations of (a) 10 h and (b) 15 h.

For the 10-h intervention, the region of reduced final coverage is comparatively narrow and therefore requires a more precise combination of onset time and sufficient suppression

intensity. For the 15-h intervention, the low-coverage region becomes substantially broader, especially across intermediate onset times, indicating that the longer intervention relaxes the requirement for precise temporal placement. At the same time, increasing D_{amount} beyond the moderate-intensity range produces progressively smaller additional changes in coverage. The qualitative correspondence between Figs. 7 and 8 indicates that transient changes in AHL dynamics are associated with differences in final basal surface colonization, consistent with the modeled quorum sensing-dependent biomass redistribution mechanism.

5 Conclusion

In this work, the previously developed hybrid cellular automaton model of quorum sensing-controlled biofilm evolution was extended by introducing a transient additional AHL degradation mechanism. The proposed modification allows us to simulate a temporary disruption of bacterial signaling without directly modifying the biomass-growth law. In this formulation, the intervention changes the AHL field and therefore affects biofilm development through the quorum sensing dependent biomass redistribution mechanism. This is of interest because it allows the effects of signal disruption to be separated from direct bactericidal or growth-inhibitory effects. The computational algorithm was modified accordingly by adding a time-dependent degradation stage to the simulation cycle while preserving nutrient and AHL transport, biomass growth, signal production, and redistribution rules. The model was implemented in C# within the Unity environment, where the developed software supports repeated stochastic simulations and systematic variation of intervention parameters.

The numerical experiments show that the response of the model is determined not only by the magnitude of additional AHL degradation but also by its temporal relation to the natural development of the signaling field. Interventions applied during an intermediate stage of biofilm development produce the most pronounced changes in cumulative AHL exposure and bottom-surface coverage, whereas very early or late interventions are less effective within the considered parameter range. Increasing the intervention duration makes the response less sensitive to the exact starting time, while further increases in degradation rate above a moderate level lead to comparatively smaller additional changes. The correspondence between the AHL and surface-coverage response maps indicates that transient changes in signaling dynamics can influence subsequent basal surface colonization. The representative spatial snapshots complement this quantitative measure by illustrating the distribution of biomass within the computational domain. This timing dependence is consistent with a broader feature of biofilm-control strategies: the effect of an external treatment may depend strongly on the physiological and developmental state of the biofilm at the moment of intervention. Similar timing-sensitive effects have been reported for antimicrobial and bacteriophage treatments, although the underlying mechanisms differ from the QS-targeted mechanism considered here. In the present model, the relevant temporal reference is the development of the AHL signaling field, suggesting that the relation between treatment time and QS dynamics may be as important as treatment intensity itself.

Further development of the model may include a more detailed representation of quorum-quenching mechanisms, comparison of different types and schedules of transient interventions, and calibration against experimental measurements of signaling and biofilm morphology. Extending the framework to three-dimensional domains would also make it possible to study spatial structures that cannot be represented in a two-dimensional lattice. Another direction is the analysis of multispecies biofilms and more complex signaling interactions, together with further optimization of the numerical algorithms for large parameter studies and three-dimensional simulations.

References

[1] E. Alpkvist, C. Picioreanu, M. C. M. van Loosdrecht, and A. Heyden. Three-dimensional biofilm model with individual cells and continuum EPS matrix. *Biotechnology and Bioengineering*, 94:961–979, 2006.

[2] J. D. Dockery and J. P. Keener. A mathematical model for quorum sensing in *Pseudomonas aeruginosa*. *Bulletin of Mathematical Biology*, 63(1):95–116, 2001.

[3] Y.-H. Dong, L.-H. Wang, J.-L. Xu, H.-B. Zhang, X.-F. Zhang, and L.-H. Zhang. Quenching quorum-sensing-dependent bacterial infection by an N-acyl homoserine lactonase. *Nature*, 411(6839):813–817, 2001.

[4] R. M. Donlan and J. W. Costerton. Biofilms: Survival mechanisms of clinically relevant microorganisms. *Clinical Microbiology Reviews*, 15(2):167–193, 2002.

[5] K. Drescher, J. Dunkel, C. D. Nadell, S. van Teeffelen, I. Grnja, N. S. Wingreen, H. A. Stone, and B. L. Bassler. Architectural transitions in *Vibrio cholerae* biofilms at single-cell resolution. *Proceedings of the National Academy of Sciences of the United States of America*, 113(14):E2066–E2072, 2016.

[6] H. J. Eberl, C. Picioreanu, J. J. Heijnen, and M. C. M. van Loosdrecht. A three-dimensional numerical study on the correlation of spatial structure, hydrodynamic conditions, and mass transfer and conversion in biofilms. *Chemical Engineering Science*, 55:6209–6222, 2000.

[7] H.-C. Flemming, J. Wingender, U. Szewzyk, P. Steinberg, S. A. Rice, and S. Kjelleberg. Biofilms: An emergent form of bacterial life. *Nature Reviews Microbiology*, 14:563–575, 2016.

[8] H.-C. Flemming and S. Wuertz. Bacteria and archaea on earth and their abundance in biofilms. *Nature Reviews Microbiology*, 17:247–260, 2019.

[9] C. Grandclement, M. Tannieres, S. Morera, Y. Dessaux, and D. Faure. Quorum quenching: Role in nature and applied developments. *FEMS Microbiology Reviews*, 40(1):86–116, 2016.

[10] L. Hall-Stoodley, J. W. Costerton, and P. Stoodley. Bacterial biofilms: From the natural environment to infectious diseases. *Nature Reviews Microbiology*, 2:95–108, 2004.

[11] J.-U. Kreft, C. Picioreanu, J. W. T. Wimpenny, and M. C. M. van Loosdrecht. Individual-based modelling of biofilms. *Microbiology*, 147:2897–2912, 2001.

[12] C. Kuttler and A. Maslovskaya. Hybrid stochastic fractional-based approach to modeling bacterial quorum sensing. *Applied Mathematical Modelling*, 93:360–375, 2021.

[13] C. Kuttler and A. Maslovskaya. Computer-assisted modeling of quorum sensing in bacterial population exposed to antibiotics. *Frontiers in Applied Mathematics and Statistics*, 8:951783, 2022.

[14] J. Lee and L. Zhang. The hierarchy quorum sensing network in *Pseudomonas aeruginosa*. *Protein & Cell*, 6:26–41, 2015.

[15] S. Mukherjee and B. L. Bassler. Bacterial quorum sensing in complex and dynamically changing environments. *Nature Reviews Microbiology*, 17:371–382, 2019.

[16] E. Paluch, J. Rewak-Soroczynska, I. Jedrusik, E. Mazurkiewicz, and K. Jermakow. Prevention of biofilm formation by quorum quenching. *Applied Microbiology and Biotechnology*, 104:1871–1881, 2020.

[17] K. Papenfort and B. L. Bassler. Quorum sensing signal–response systems in gram-negative bacteria. *Nature Reviews Microbiology*, 14:576–588, 2016.

[18] J. Perez-Velazquez, M. Gogeli, and R. Garcia-Contreras. Mathematical modelling of bacterial quorum sensing: A review. *Bulletin of Mathematical Biology*, 78(8):1585–1639, 2016.

[19] C. Picioreanu, M. C. M. van Loosdrecht, and J. J. Heijnen. Mathematical modeling of biofilm structure with a hybrid differential-discrete cellular automaton approach. *Biotechnology and Bioengineering*, 58(1):101–116, 1998.

[20] D. Rodriguez, B. Einarsson, and A. Carpio. Biofilm growth on rugose surfaces. *Physical Review E*, 86:061914, 2012.

[21] S. T. Rutherford and B. L. Bassler. Bacterial quorum sensing: Its role in virulence and possibilities for its control. *Cold Spring Harbor Perspectives in Medicine*, 2:a012427, 2012.

[22] S. Sarukhanian, C. Kuttler, and A. Maslovskaya. Hybrid cellular automaton-based model for quorum sensing-controlled biofilm evolution. *Computers in Biology and Medicine*, 213:111852, 2026.

[23] S. Sarukhanian, A. Maslovskaya, and C. Kuttler. Three-dimensional cellular automaton for modeling of self-similar evolution in biofilm-forming bacterial populations. *Mathematics*, 11(15):3346, 2023.

[24] P. S. Stewart and M. J. Franklin. Physiological heterogeneity in biofilms. *Nature Reviews Microbiology*, 6:199–210, 2008.

[25] J. P. Ward, J. R. King, A. J. Koerber, P. Williams, J. M. Croft, and R. E. Sockett. Mathematical modelling of quorum sensing in bacteria. *IMA Journal of Mathematics Applied in Medicine and Biology*, 18(3):263–292, 2001.

[26] C. M. Waters and B. L. Bassler. Quorum sensing: Cell-to-cell communication in bacteria. *Annual Review of Cell and Developmental Biology*, 21:319–346, 2005.